Multiple-q states of the J_1-J_2 classical honeycomb-lattice Heisenberg antiferromagnet under a magnetic field

Tokuro Shimokawa,[1,*] Tsuyoshi Okubo,[2] and Hikaru Kawamura[3]

[1]*Theory of Quantum Matter Unit, Okinawa Institute of Science and Technology Graduate University, Onna-son, Okinawa 904-0412, Japan*

[2]*Department of Physics, University of Tokyo, Tokyo 113-0033, Japan*

[3]*Department of Earth and Space Science, Graduate School of Science, Osaka University, Toyonaka, Osaka 560-0043, Japan*

(Received 5 February 2019; revised manuscript received 27 September 2019; published 2 December 2019)

Motivated by the recent theoretical study by Okubo *et al.* [Phys. Rev. Lett. **108**, 017206 (2012)] on the possible realization of the frustration-induced *symmetric* skyrmion-lattice state in the J_1-J_2 (or J_1-J_3) triangular-lattice Heisenberg model without the Dzyaloshinskii-Moriya interaction, we investigate the ordering of the classical J_1-J_2 honeycomb-lattice Heisenberg antiferromagnet under a magnetic field by means of a Monte Carlo simulation, a mean-field analysis and a low-temperature expansion. The model has been known to have an infinite ringlike degeneracy in the wave-vector space in its ground state for $1/6 < J_2/J_1 < 0.5$, in distinction with the triangular-lattice model. As reported by Okumura *et al.* [J. Phys. Soc. Jpn. **79**, 114705 (2010)], such a ringlike degeneracy gives rise to exotic spin liquid states in zero field, e.g., the "ring-liquid" state and the "pancake-liquid" state. In this paper, we study the in-field ordering properties of the model paying attention to the possible appearance of exotic multiple-q states. Main focus is made on the $J_2/J_1 = 0.3$ case, where we observe a rich variety of multiple-q states including the single-q, double-q, and triple-q states. While the skyrmion-lattice triple-q state observed in the triangular-lattice model is not realized, we instead observe an exotic double-q state consisting of meron/antimeron-like lattice textures.

DOI: 10.1103/PhysRevB.100.224404

I. INTRODUCTION

Frustrated spin systems have attracted much interest in the field of magnetism. One of such research interest might be that novel types of ordering are often generated by the effects of quantum or thermal fluctuations on the highly degenerate classical ground states. The so-called "order-by-disorder" mechanism often comes into play [1–4].

An intriguing example of such frustrated magnets with heavily degenerate classical ground-state manifold might be the antiferromagnetic (AF) Heisenberg model on a honeycomb lattice with the competing nearest-neighbor (NN) J_1 and next-nearest-neighbor (NNN) J_2 couplings as illustrated in Fig. 1.

Essentially, the ratio of these coupling parameters J_2/J_1 determines the nature of the ground state. For smaller $J_2/J_1 \leqslant 1/6$ where the frustration is relatively weak, a simple AF order is stabilized in the ground state by reflecting the bipartite character of the honeycomb lattice. For larger $J_2/J_1 > 1/6$, the ground state becomes a helical or spiral state characterized by a single wave vector $\mathbf{q}$ which is generally incommensurate with the underlying honeycomb lattice [5], a single-q state. An interesting feature here is that the ground-state manifold possesses a macroscopic degeneracy associated with the running directions of the wave vector $\mathbf{q}$. In the wave-vector space, the set of the ground-state q's forms a closed curve surrounding the origin in the sublattice wave-vector space. For $1/6 < J_2/J_1 < 0.5$, this closed curve looks like a "ring" as demonstrated in Fig. 2. This "ringlike" degeneracy could give rise to a variety of unique ordering properties [6,7]. In fact, the effects of thermal and quantum fluctuations in this J_1-J_2 honeycomb-lattice model have recently been investigated quite intensively [6–25].

One candidate material of the J_1-J_2 honeycomb-lattice Heisenberg model might be the $S = 3/2$ compound $Bi_3Mn_4O_{12}(NO_3)$ [26–31]. This compound exhibits a spin-liquidlike behavior without any magnetic long-range order (LRO) down to 0.4 K in spite of a large absolute value of Weiss temperature, $\sim$257 K. Furthermore, neutron-scattering measurements have revealed that it exhibits a field-induced antiferromagnetism, i.e., a metamagnetic transition occurs even under a relatively weak field [27].

Such unique features of $Bi_3Mn_4O_{12}(NO_3)$ including the spin-liquid behavior and the field-induced antiferromagnetism were theoretically investigated by Okumura, Kawamura, Okubo, and Motome by a Monte Carlo (MC) simulation and a low-temperature expansion [6]. They have found that the energy scale of the order-by-disorder is suppressed near the AF phase boundary ($J_2/J_1 = 1/6$) down to extremely low temperatures, and the two kinds of exotic spin-liquid states, which are called "ring-liquid" and "pancake-liquid" states, appear in the low-temperature region. The spin structure factor in the former state exhibits a ringlike pattern surrounding the origin in the sublattice wave-vector space, while, in the spin structure factor in the latter state, the center of the ringlike pattern is "buried" in intensity, yielding a "pancakelike" pattern. The ring radius of the spin structure

*tokuro.shimokawa@oist.jp

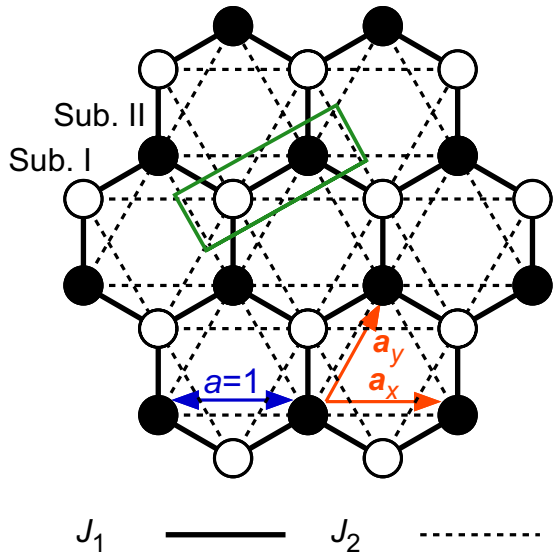

FIG. 1. The J_1-J_2 honeycomb model with a trigonal symmetry, where J_1 and J_2 represent the nearest-neighbor (black solid line) and the next-nearest-neighbor (black dot line) interactions. The lattice constant of the triangular lattice a, which is equal to the next-nearest-neighbor distance of the honeycomb lattice, is taken to be the length unit, i.e., $a = 1$. Unit vectors on the triangular lattice are $\mathbf{a}_x = (a, 0)$ and $\mathbf{a}_y = (\frac{a}{2}, \frac{\sqrt{3}a}{2})$. The honeycomb lattice has two lattice sites in a unit cell belonging to two triangular sublattices, which we denote I (white site) and II (black site). Our choice of the unit cell is indicated by the green box. The shape of the honeycomb cluster we mainly treat in this study is a hexagonal one with the trigonal symmetry. The depicted cluster contains 24 spins ($L = 4$) under open boundary conditions.

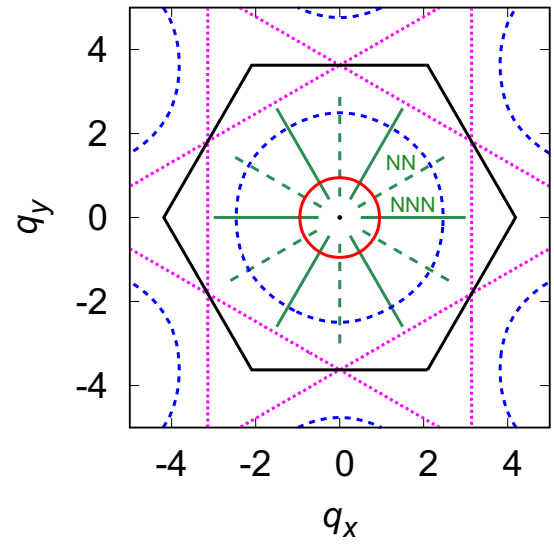

FIG. 2. The ground-state manifold of the J_1-J_2 classical honeycomb-lattice Heisenberg antiferromagnet in the sublattice wave-vector space. The red, blue, and purple lines represent the degenerate lines for $J_2/J_1 = 0.18$, 0.3, and 0.5, respectively. Black point is located at the origin. Note that the origin corresponds to the wave-vector point having a simple two-sublattice Neel order on the original honeycomb lattice. Black solid hexagon indicates the first Brillouin zone of the triangular sublattice. Green dotted and solid lines show the NN and NNN directions, respectively.

factor just corresponds to the radius of the degenerate ring (closed curve) of the ground-state manifold. Okumura *et al* discussed the possible relationship of these ring-liquid and pancake-liquid states to the experimental properties of $Bi_3Mn_4O_{12}(NO_3)$, and emphasized the crucial importance of the ringlike degeneracy, which is a source of various exotic spin-liquidlike behaviors and the field-induced antiferromagnetism. At low enough temperatures, the mechanism of order by disorder works, leading to an entropic selection of a particular $\mathbf{q}$ on the degenerate ring and to a thermodynamic phase transition into the symmetry-broken single-q spiral state.

Frequently, an incommensurate ordering, as often realized in the frustrated classical J_1-J_2 model, gives rise to a variety of multiple-q states, especially under the applied magnetic field [19,32–41]. The multiple-q state is a coherent superposition of states with equivalent but distinct wave vectors related by the underlying symmetry of the lattice.

For the J_1-J_2 Heisenberg model on the triangular lattice under a magnetic field, Okubo, Chung, and Kawamura identified a variety of multiple-q states including single-q, double-q, and triple-q states. Especially interesting might be the triple-q state, which corresponds to the *skyrmion-lattice* state. There, the skyrmion lattice is solely stabilized by the *symmetric* exchange interaction, and hence, in contrast to the standard skyrmion lattice stabilized by the antisymmetric Dzyaloshinskii-Moriya (DM) interaction, the skyrmion with an opposite sense of the skyrmion number or the spin scalar chirality, i.e., the antiskyrmion, is also possible.

Emergence of such multiple-q states are naturally expected for incommensurate orderings on other lattices as well, e.g., the honeycomb lattice possessing a common trigonal symmetry with the triangular lattice. On the basis of such an expectation, we study in the present paper the ordering properties of the classical J_1-J_2 honeycomb-lattice AF Heisenberg model under a magnetic field. As emphasized above, unique feature of the honeycomb-lattice model might be that it exhibits a ringlike continuous degeneracy in its ground state in sharp contrast to the triangular-lattice model, which might give rise to still exotic multiple-q ordered states different from the ones identified in the triangular-lattice model. With this expectation, we study here the J_1-J_2 honeycomb model in the parameter range of $1/6 < J_2/J_1 < 0.5$ where the ground state of the model exhibits a ringlike infinite degeneracy. As shown in Fig. 2, this ring gets closer to a true circle as $J_2/J_1 \to 1/6$ while its shape tends to deviate more from a true circle for larger J_2/J_1.

Main focus of our simulation is on the case of $J_2/J_1 = 0.3$, which is located in the middle of the paramagnetic (ring-liquid)-helical phase boundary [6]. At this value of J_2/J_1, the degenerate ring is still close to a true circle (see Fig. 2). Its radius is $q^* \simeq 2.494$ in the NN direction, and is is $q^* \simeq 2.462$ in the NNN direction. When the associated ordered state is to be a single-q spiral state, this q-value corresponds to a turn angle on the triangular sublattice of 0.794π (NN), or of 0.784π (NNN), respectively.

For this value of $J_2/J_1 = 0.3$, we indeed find a variety of novel multiple-q ordered states there, many of which

differs in nature from the ones identified in the triangular J_1-J_2 model. In particular, we observe three different types of double-q state, one of which is essentially of the same nature as the double-q state identified in the triangular model, while the other two are new ones. One is a coplanar state, and the other is a noncoplanar state where the spins form interweaving "meronlike" vortex/antivortex lattice pattern. By contrast, only one type of triple-q state is stabilized, which is a collinear state distinct from the skyrmion-lattice state. The triple-q (collinear) state is adiabatically identical with the "Z state" identified in the triangular model. Meanwhile, the transverse spin correlation length stays very short in the triple-q (collinear) state of the present model so that the state does not look like the random-domain state consisting of skyrmion and antiskyrmion lattices as observed in the Z phase of the triangular model.

Concerning the single-q states, we find two types, the umbrella (spiral)-type and the fan-type, the latter stabilized only in higher magnetic field. For the umbrella-type single-q state, we observe a switching of the running direction of the associated $\mathbf{q}$ vector with varying the magnetic-field intensity and the temperature. For fuller understanding of the ordering process of the model, we also investigate other J_2/J_1-values including $J_2/J_1 = 0.20, 0.25, 0.35$ and 0.45.

The present paper is organized as follows. In Sec. II, we present our model and explain the numerical and theoretical methods employed. Section III is the main part of the present paper, and is devoted to the presentation of the results of our MC simulations on the model with $J_2/J_1 = 0.3$. In Sec. IV, we deal with the other J_2/J_1 values, $J_2/J_1 = 0.20, 0.25, 0.35$ and 0.45. We summarize our main findings in Sec. V. Details of the low-temperature expansion are given in Appendix A, whereas some additional information about the triple-q (collinear, type 2) state stabilized at $J_2/J_1 = 0.45$ is given in Appendix B. In order to get some insights into the relative stability of various multiple-q states, we perform a mean-field (MF) analysis of the model, and compare the results with the MC results. The details are given in Ref. [42].

II. MODEL AND METHOD

We consider the J_1-J_2 classical honeycomb-lattice Heisenberg model in a magnetic field of intensity H, whose Hamiltonian is given by

$$\mathcal{H} = -J_1 \sum_{\langle i,j \rangle} \mathbf{S}_i \cdot \mathbf{S}_j - J_2 \sum_{\langle\langle i,j \rangle\rangle} \mathbf{S}_i \cdot \mathbf{S}_j - H \sum_i S_i^z, \qquad (1)$$

where $\mathbf{S}_i = (S_i^x, S_i^y, S_i^z)$ is the classical Heisenberg spin with the fixed length of $|\mathbf{S}_i| = 1$ located at the ith site on the honeycomb lattice, $J_1 < 0$ and $J_2 < 0$ represent the antiferromagnetic NN and NNN interactions, while the $\sum_{\langle i,j \rangle}$ and $\sum_{\langle\langle i,j \rangle\rangle}$ are taken over all NN and NNN pairs, respectively.

It has been known that the ground state of the model in zero field exhibits a single-q helical order for $J_2/J_1 > 1/6$, with an incommensurate wave vector with an infinite ringlike degeneracy in the q space, while the standard two-sublattice antiferromagnetic order arises for $J_2/J_1 \leqslant 1/6$ [5].

In general, the multiple-q states are incompatible with the fixed spin-length condition $|\mathbf{S}_i|$=1 imposed in the ground state, and are not favored in the low temperature region in the classical Heisenberg spin system. Indeed, the multiple-q states have not been reported in previous zero-field calculations of the present model, only a single-q spiral state stabilized with a wave vector selected from the degenerate ring by thermal fluctuations, breaking the threefold discrete C_3 lattice symmetry [6]. In the present paper, we wish to investigate by means of a MC simulation the possible emergence of the multiple-q states at moderate temperatures under a magnetic field.

MC simulations are performed on the basis of the standard heat-bath method combined with the over-relaxation [43,44] and temperature-exchange [45] methods. Our unit MC step consists of one heat-bath sweep and 5–10 over-relaxation sweeps. Typically, our MC runs contain $\sim 10^7$ MC steps, and averages are made over three independent runs in most cases. In computing certain physical quantities such as the spin structure factor, the temperature-exchange process is stopped to appropriately monitor the symmetry-breaking pattern.

We treat mainly hexagonal finite-size clusters with a trigonal symmetry as illustrated in Fig. 1 under open boundary conditions. Due to the enhanced effects of incommensurability, we check the stability of our results also by employing the diamond-shape clusters under periodic boundary conditions. The hexagonal clusters contain N=$(3/2)L^2$ spins, where N is the total number of spins on the honeycomb lattice, and we treat the range of sizes $36 \leqslant L \leqslant 300$.

In order to get information about the wave vector of the relevant single-q state at low temperatures, we also employ the low-temperature expansion technique [4,6]. The details of the calculation are given in Appendix A. In order to get information about the possible multiple-q ordered states of the model, we also perform the mean-field (MF) analysis. Our MF analysis is the Landau-type free energy expansion up to quartic order following the method of Reimers *et al.* [46] and of Okubo *et al.* [32,33]. The details are shown in Ref. [42].

III. MONTE CARLO RESULTS FOR $J_2/J_1 = 0.3$

In this section, we present our MC results. We focus here on the case of $J_2/J_1 = 0.3$ to study typical ordering patterns arising from the ring-liquid paramagnetic state. As has been demonstrated in the zero-field calculation of Ref. [6], the ordered state in zero-field is always a single-q spiral state, not the multiple-q states. The single-q spiral state is generated with a wave vector selected from the degenerate ringlike manifold via the order-by-disorder mechanism, breaking the C_3 lattice symmetry of the Hamiltonian. For $J_2/J_1 = 0.3$, the transition temperature is located at $T/|J_1| \simeq 0.0405$ [6]. In this section, we construct a phase diagram in the temperature (T) versus magnetic-field (H) plane at $J_2/J_1 = 0.3$.

The obtained T-H phase diagram is shown in Fig. 3. In addition to the single-q states, various types of multiple-q states, including the three distinct types of double-q states and one triple-q state, are also stabilized under the magnetic field due to thermal fluctuations.

In this phase diagram, the transition points are determined mainly from the peak position of the specific heat. As an example, we show in Fig. 4(a) the temperature and size dependence of the specific heat at $H/|J_1| = 1.5$. Three sharp

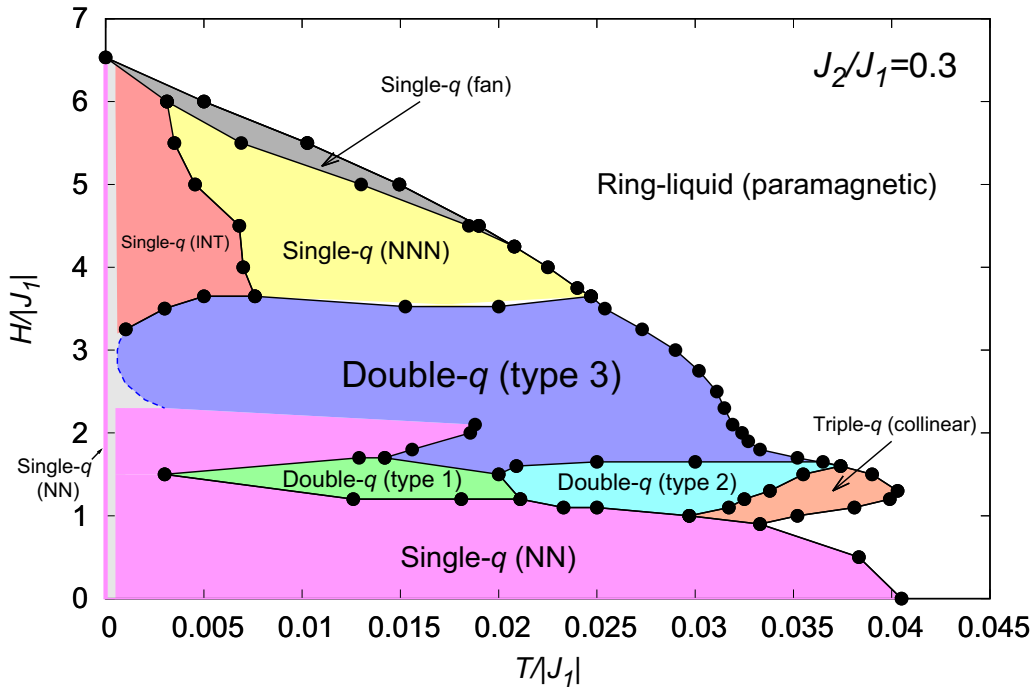

FIG. 3. The H-T phase diagram of the J_1-J_2 honeycomb-lattice Heisenberg model with $J_2/J_1 = 0.3$ determined by MC simulations. Transition points are determined from the specific-heat peak, the anomaly in the threefold symmetry order parameter m_3, and that in the magnetic susceptibility (see also Figs. 4 and 5). The low-temperature light-gray region is the region where the thermalization cannot be achieved, while the zero-temperature limit can be identified based on the low-temperature expansion as a single-q (NN) state. The dotted blue line representing the low-temperature phase boundary of the double-q (type 3) state remains somewhat arbitrary. The details of each phase are explained in the main text.

peaks appear, each of which corresponds, from high to low temperatures, to the transition from the ring-liquid paramagnetic to the triple-q (collinear) states, to the one from the triple-q (collinear) to the double-q (type 2) states, and to the one from the double-q (type 2) to the double-q (type 1) states. Other quantities such as the m_3 order parameter describing the C_3 lattice-rotational-symmetry breaking are also employed, m_3, which is defined by

$$m_3 = \langle |\mathbf{m}_3| \rangle, \quad \mathbf{m}_3 = \epsilon_1 \mathbf{e}_1 + \epsilon_2 \mathbf{e}_2 + \epsilon_3 \mathbf{e}_3, \tag{2}$$

where $\mathbf{e}_1 = (0, 1)$, $\mathbf{e}_2 = (-\sqrt{3}/2, -1/2)$, and $\mathbf{e}_3 = (\sqrt{3}/2, -1/2)$, $\epsilon_{1,2,3}$ are the total NN bond energy normalized per bond along the three NN directions, respectively, and $\langle \cdots \rangle$ is a thermal average. As can be seen from Fig. 4(b), a transition associated with the C_3 symmetry breaking is expected at $T/|J_1| \simeq 0.035$, which coincides with the second peak of the specific heat in Fig. 4(a). Although a sharp diverging peak of the specific heat, possibly corresponding to a first-order phase transition, is observed at a higher temperature $T/|J_1| \simeq 0.039$, the m_3 order parameter in the thermodynamic limit still remains to be vanishing there, meaning that the transition at $T/|J_1| \simeq 0.039$ is the one keeping the C_3 symmetry, i.e., the transition into the triple-q (collinear) state in the phase diagram of Fig. 3.

Sometimes, the phase boundary happens to be almost temperature-independent, i.e., almost horizontal in the T-H phase diagram. In such a case, the magnetic field dependence of physical quantities could also be useful in determining the phase boundary. As an example, we show in Figs. 5(a) and 5(b) the magnetic-field dependence of (a) the xy and z components of the differential magnetic susceptibility, and (b) the m_3 order parameter, which turn out to be useful in locating the phase boundary between the double-q (type 2) and (type 3) states as indicated by the arrow in the figure.

A convenient quantity in identifying various types of multiple-q ordered states might be the static spin structure factor. In the present paper, in view of the basic two-sublattice (I or II) nature of the ordering, we compute primarily the *sublattice* spin structure factor, both perpendicular to the field (the xy component) and parallel with the field (the z component). Note that the honeycomb lattice contains two lattice points in its unit cell, each forming a triangular sublattice whose unit lattice vector corresponds to the NNN direction of the original honeycomb lattice: see Fig. 1.

The xy component of the sublattice spin structure factor $S_\perp(\mathbf{q})$ is defined by

$$S_\perp(\mathbf{q}) = \frac{2}{N} \sum_{\mu=x,y} \left\langle \left| \sum_{j \in \text{I or II}} S_j^\mu e^{-i\mathbf{q}\cdot\mathbf{r}_j} \right|^2 \right\rangle, \tag{3}$$

while the z component $S_\parallel(\mathbf{q})$ by

$$S_\parallel(\mathbf{q}) = \frac{2}{N} \left\langle \left| \sum_{j \in \text{I or II}} S_j^z e^{-i\mathbf{q}\cdot\mathbf{r}_j} \right|^2 \right\rangle, \tag{4}$$

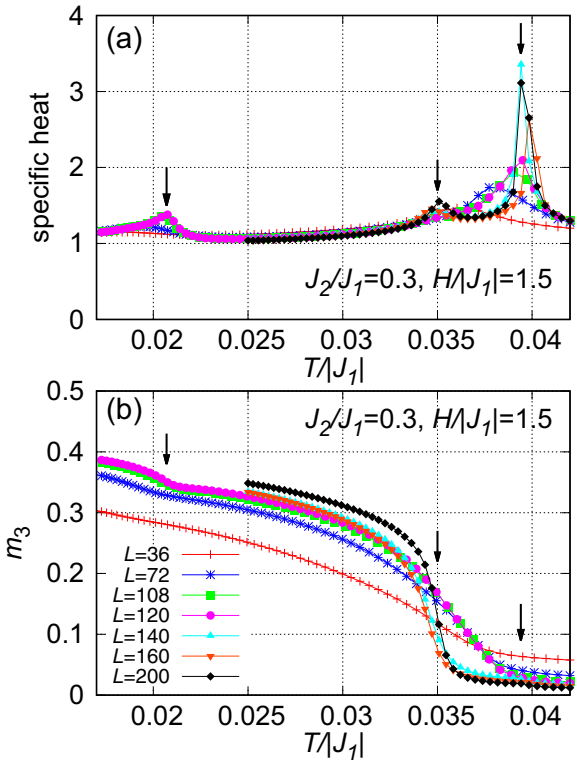

FIG. 4. The temperature dependence of the physical quantities employed in drawing the phase diagram of Fig. 3, i.e., (a) the specific heat per spin, and (b) the m_3 order parameter. The magnetic-field intensity is $H/|J_1| = 1.5$. Arrows indicate the transition points.

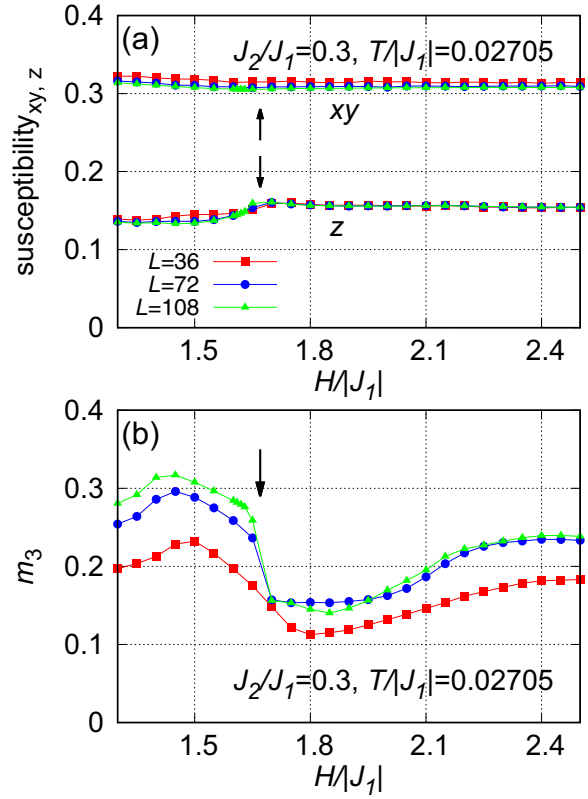

FIG. 5. The field dependence of the physical quantities employed in drawing the phase diagram of $J_2/J_1 = 0.30$, i.e., (a) the xy and z components of the magnetic susceptibility, and (b) the m_3 order parameter. The temperature is $T/|J_1| = 0.02705$. Arrows indicate the transition point.

where $\mathbf{r}_j$ is the position vector of the spin at the jth site on each triangular sublattice, and $\mathbf{q} = (q_x, q_y)$ is the associated wave vector. Thus, in our present definition of the q vector, the $\mathbf{q} = (0, 0)$ point corresponds to the wave-vector point associated with the two-sublattice Neel order on the original honeycomb lattice. In any finite-size simulation, fully symmetric patterns should be obtained in the spin structure factor when the system is fully thermalized, whereas in the ordered state, such a timescale usually becomes extremely long for a moderately large system. Hence, in computing the spin structure factor in our present MC simulation, we turn off the temperature-exchange process, and monitor the symmetry-breaking pattern typically during $10^3 \sim 10^4$ MC steps for the measurements.

A. The ring-liquid (paramagnetic) states

In Fig. 6, we show the intensity plots of the sublattice static spin structure factor in the ring-liquid paramagnetic state. As can be seen from the figure, $S_\perp(\mathbf{q})$ exhibits a broad ringlike intensity, while $S_\parallel(\mathbf{q})$ exhibits a sharp peak only at $q = 0$ arising from the uniform magnetization induced by an applied magnetic field. This ringlike intensity reflects the ringlike degeneracy of the ground state as argued above. On decreasing the temperature, various types of ordered states including multiple-q states could emerge by selecting various wave vectors from the ringlike degenerate manifold. In this sense, the ring serves as a source of various multiple-q states to be discussed below.

B. The single-q states

The single-q state is characterized by one of the incommensurate wave vectors on the ring, $\mathbf{q}^*$, and its partner $-\mathbf{q}^*$. In fact, there exist several different types of single-q states under the magnetic field at $J_2/J_1 = 0.3$, such as the single-q (NN), the single-q (NNN), the single-q (INT), and the single-q (fan) states. The former two states were already mentioned in the Introduction and reported in Ref. [6]. The single-q (NN, NNN, and INT) states have umbrella-type spin textures, while the single-q (fan) state has a different type of spin texture, a fanlike coplanar structure, as will be explained below.

In the single-q (NN) state, the spiral axis runs along the NN direction of the honeycomb lattice. As can be seen from the phase diagram of Fig. 3, this state is realized at the relatively low magnetic field including zero magnetic field. In fact, this observation is fully consistent with the previous finding of Okumura *et al.* that the spiral runs along the NN direction in zero field for $J_2/J_1 = 0.3$ [6].

We show in Figs. 7(a) and 7(b) the typical sublattice spin structure factors for the single-q (NN) state. Sharp peaks appear in the transverse component $S_\perp(\mathbf{q})$ at a pair of $\pm\mathbf{q}^*$, while broader peaks appear in the longitudinal component $S_\parallel(\mathbf{q})$ at the same wave-vector points $\pm\mathbf{q}^*$, in addition to the uniform component at $\mathbf{q} = \mathbf{0}$ induced by an applied field. The broad peaks of $S_\parallel(\mathbf{q})$ do not sharpen with increasing the system size, indicating the short-ranged-order (SRO) character

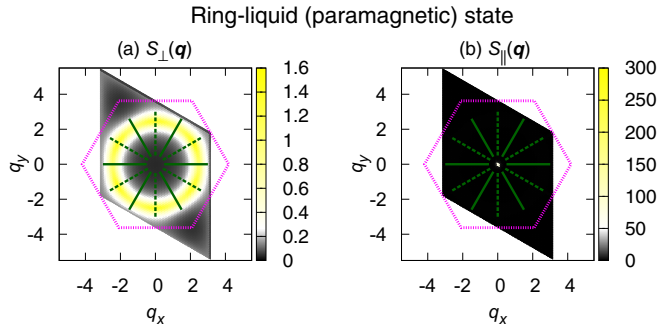

FIG. 6. The intensity plots of the sublattice spin structure factors in the wave-vector (q_x, q_y) plane in the ring-liquid paramagnetic state: (a) the transverse component $S_\perp(\mathbf{q})$ and (b) the longitudinal component $S_\parallel(\mathbf{q})$. The parameters are $J_2/J_1 = 0.3$, $H/|J_1| = 2.50$, and $T/|J_1| = 0.042$, for the lattice size $L = 72$. The length unit is taken to be the NNN distance of the honeycomb lattice (or the NN distance of the triangular sublattice). The dotted purple line depicts the zone boundary of the first Brillouin zone of the triangular sublattice. The NN (NNN) directions of the honeycomb lattice are given by the green broken (solid) lines.

of the z component. In contrast, the sharp feature of $S_\perp(\mathbf{q})$ is consistent with the expected quasi-LRO character of the single-q spiral structure.

Stronger magnetic field can produce a single-q spiral running along the NNN directions, which we denote as a single-q (NNN) state as shown in Fig. 3. The corresponding spin structure factors are shown in Figs. 7(c) and 7(d). In contrast to sharp peaks of $S_\perp(\mathbf{q})$, weak broad peaks appear in $S_\parallel(\mathbf{q})$ at the wave vectors complementary to the strong spots in $S_\perp(\mathbf{q})$.

We note that, in the lower temperature region and in stronger magnetic field, the single-q spiral runs along an intermediate direction between the NN and the NNN ones, which we denote as a single-q (INT) state. The corresponding spin structure factor is shown in Figs. 7(e) and 7(f).

Thus, depending on T and H, the single-q spiral can run in various directions, while any direction can be selected from the q directions on the degenerate ring. In order to understand the selection mechanism of a particular q direction, i.e., the "order-by-disorder" mechanism operating here, we employ the low-temperature expansion calculations of Refs. [4,6] by extending their zero-field calculations to a nonzero field. Note that the low-temperature expansion is completely independent of our MC calculation, no input provided from MC. Some of the details are explained in Appendix A. We find that, at $J_2/J_1 = 0.30$, thermal fluctuations always select the NN direction at low enough temperatures for any H. In Fig. 8, we show for $J_2/J_1 = 0.30$ the directional dependence of the free-energy density difference between a given spiral state with the wave vector $\mathbf{q}^*$ lying on the degenerate ring (see black points in the inset of Fig. 8) and the spiral running along the NN direction, $\Delta F/T \equiv F(\mathbf{q}^*)/T - F(\mathbf{q}^*_{\rm NN})/T$, computed based on Eqs. (A9)–(A11). As can be seen from the figure, ΔF is always positive, indicating that thermal fluctuations prefer the NN direction in the low-temperature limit $T/|J_1| \to 0$ among all possible directions on the degenerate ring.

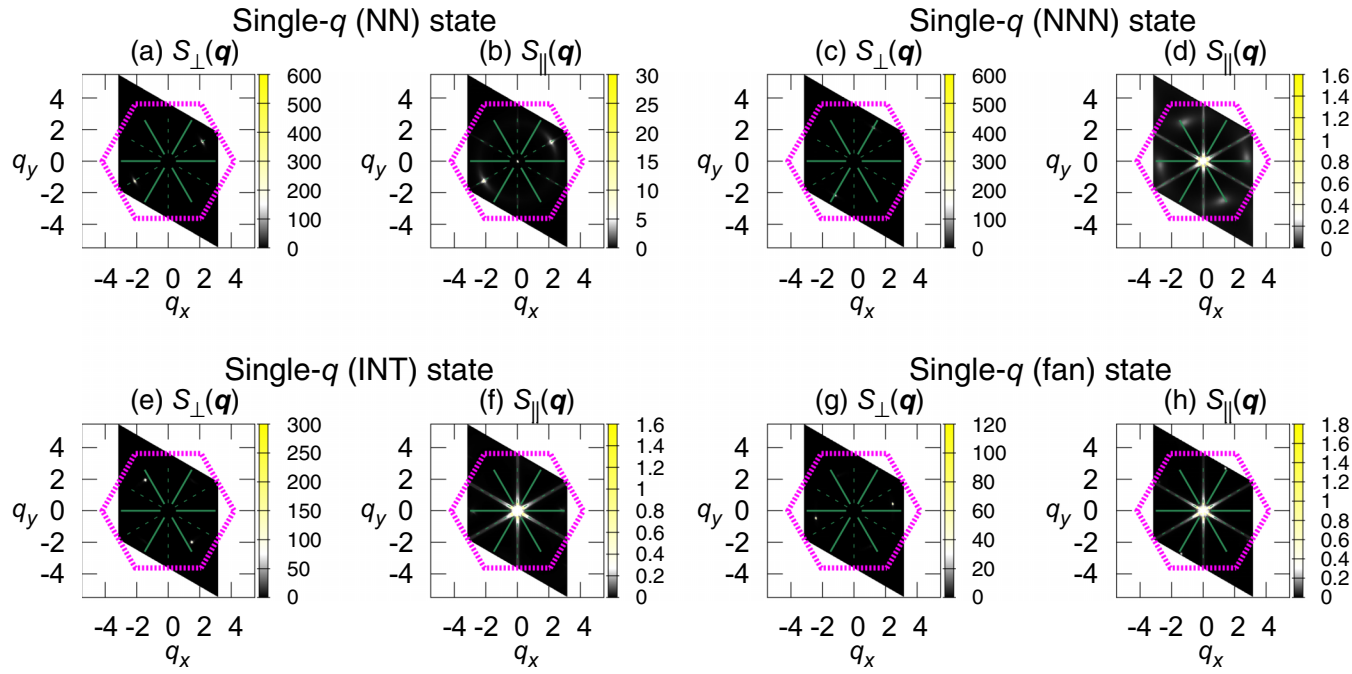

FIG. 7. The intensity plots of the sublattice spin structure factors in the wave-vector (q_x, q_y) plane for various single-q states realized for $J_2/J_1 = 0.3$. (a) and (b) correspond to the single-q (NN) state at $H/|J_1| = 0.5$, $T/|J_1| = 0.0215$, and $L = 108$, (c) and (d) to the single-q (NNN) state at $H/|J_1| = 4.0$, $T/|J_1| = 0.0182$, and $L = 120$, (e) and (f) to the single-q (INT) state at $H/|J_1| = 5.5$, $T/|J_1| = 0.003075$, and $L = 120$, and (g) and (h) to the single-q (fan) state at $H/|J_1| = 6.0$, $T/|J_1| = 0.003862$, and $L = 150$. (a), (c), (e), and (g) represent the transverse component $S_\perp(\mathbf{q})$, while (b), (d), (f), and (h) the longitudinal component $S_\parallel(\mathbf{q})$. Note that we tune the intensity range in (d), (f), and (h) to focus subtle features of the intensities on the degenerate ring except for a dominant $\mathbf{q} = \mathbf{0}$ peak.

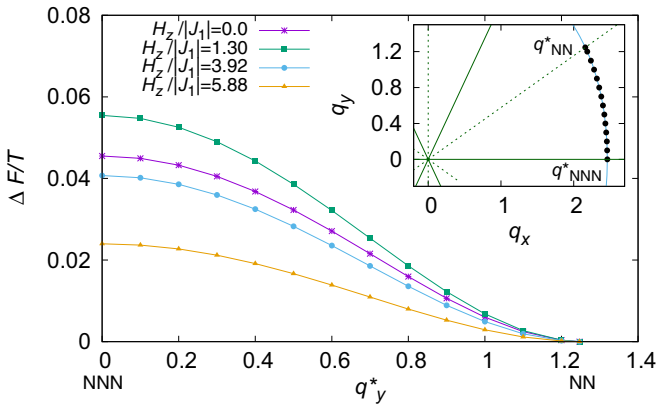

FIG. 8. The q^*-vector direction dependence of the free-energy density difference $\Delta F/T \equiv F(\mathbf{q}^*)/T - F(\mathbf{q}^*_{\rm NN})/T$ for various fields calculated by the low-temperature expansion at $J_2/J_1 = 0.30$, where the free energy density of the spiral running along the NN direction $F(\mathbf{q}^*_{\rm NN})$ is taken as an energy origin, and $\mathbf{q}^* = (q^*_x, q^*_y)$ is the wave vector on the degenerate ring (the blue line in the inset) for $J_2/J_1 = 0.3$. As depicted in the inset, the direction of the spiral is represented by its q^*_y value. The NN and the NNN directions are drawn by the green solid and broken lines, respectively.

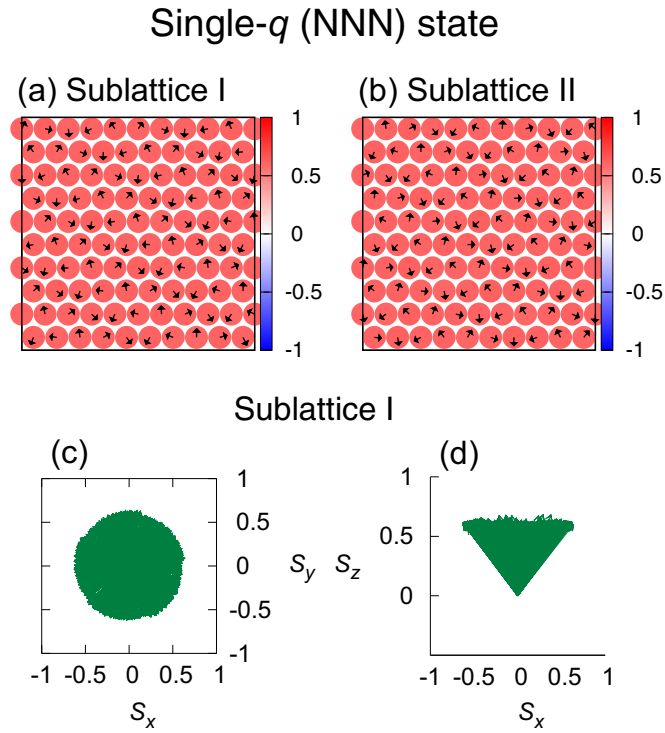

FIG. 9. Real-space sublattice spin configurations in the single-q (NNN) state for $J_2/J_1 = 0.3$ obtained by the short-time average of 1000 MC steps: (a) for the sublattice I and (b) for the sublattice II. The parameters are $H/|J_1| = 4.0$, $T/|J_1| = 0.01820$, and $L = 120$. [(a) and (b)] The xy components of the spin are represented by the arrow, while the z component is represented by the blue-to-red color scale. In (c) and (d), spins at various sites on the sublattice I are reorganized with a common origin: (c) the top view in the (S_x, S_y) plane and (d) the side view in the (S_x, S_z) plane.

At higher magnetic field of $H/|J_1| > 2.2$, the low-temperature expansion results might seem inconsistent with our MC phase diagram of Fig. 3. One possible cause of this apparent discrepancy might be a possible failure of the harmonic (Gaussian) approximation of our low-temperature expansion neglecting the nonlinear effects. Meanwhile, our MC specific-heat data at $H/|J_1| > 2.2$ take values greater than the harmonic value of unity expected for the classical Heisenberg spin systems, down to a low temperature $T/|J_1| = 0.005$. In contrast, the specific heat should take a value less than unity [47] when the nonlinear effects around the ground state are dominant. Hence, a plausible explanation here might be that an additional phase transition, most probably to the single-q (NN) state, occurs at a still lower temperature of $T/|J_1| < 0.005$. Unfortunately, we could not thermalize such a low-temperature regime in our MC.

These three types of single-q states (NN, NNN and INT) have umbrella-type structures in their real-space spin configurations. We show in Fig. 9 typical real-space sublattice spin configurations of the single-q (NNN) state: (a) for the sublattice I and (b) for the sublattice II. These real-space spin configurations correspond to the spin structure factors shown in Figs. 7(c) and 7(d). In Figs. 9(c) and 9(d), spins at various sites on the sublattice I are reorganized in the spin space with a common origin, a top view in the (S_x, S_y) plane in (c), and a side view in the (S_x, S_z) plane in (d). Essentially the same plots are obtained also for the sublattice II (not shown here). The real-space xy-spin configurations on the two sublattices look essentially similar, with a phase difference of $\alpha \sim 0.55\pi$. This value of the phase difference is a bit smaller than, but close to the corresponding value expected in the ground state for $J_2/J_1 = 0.3$, $\alpha \sim 0.61\pi$: Refer to $\alpha_{q^*_{1,\rm NNN}}$ in Fig. S1(a) of Ref. [42]. The observed small deviation is most probably the temperature effect.

In addition to such umbrella-type single-q states, the other type of single-q state also appears in the high-field region of the phase diagram just below the phase boundary to the ring-liquid paramagnetic state. In this state, as can be seen from Figs. 7(g) and 7(h), the associated ordering wave vector runs along an intermediate direction between the NN and the NNN directions like the single-q (INT) state. The real-space spin configuration has a fanlike coplanar structure, instead of the noncoplanar umbrella-type one. We call this type of single-q state a single-q (fan) state. Figure 10 exhibits the typical spin configuration of this single-q (fan) state realized at $H/|J_1| = 6.00$ and $T/|J_1| = 0.003862$ for the sublattice I in (a)–(c) and for the sublattice II in (d) and (e). As can be seen from the figures, the spin structure in the fan state is coplanar.

C. The double-q (type 1) state

The double-q structure is characterized by two pairs of $\mathbf{q}^*$ in $S_\perp(\mathbf{q})$. For $J_2/J_1 = 0.3$, three distinct types of double-q states appear. Let us begin with the double-q (type 1) state, whose sublattice spin structure factors are shown in Figs. 11(a) and 11(b). Two pairs of spot intensities appear in $S_\perp(\mathbf{q})$, while a pair of intensities appears in $S_\parallel(\mathbf{q})$ at the wave vectors complementary to the two pairs in $S_\perp(\mathbf{q})$. In this state, relevant $\mathbf{q}^*$ vectors run along the NN direction. The reason why the $\mathbf{q}^*$ vectors run along the NN directions will be discussed within the MF analysis (see Ref. [42]).

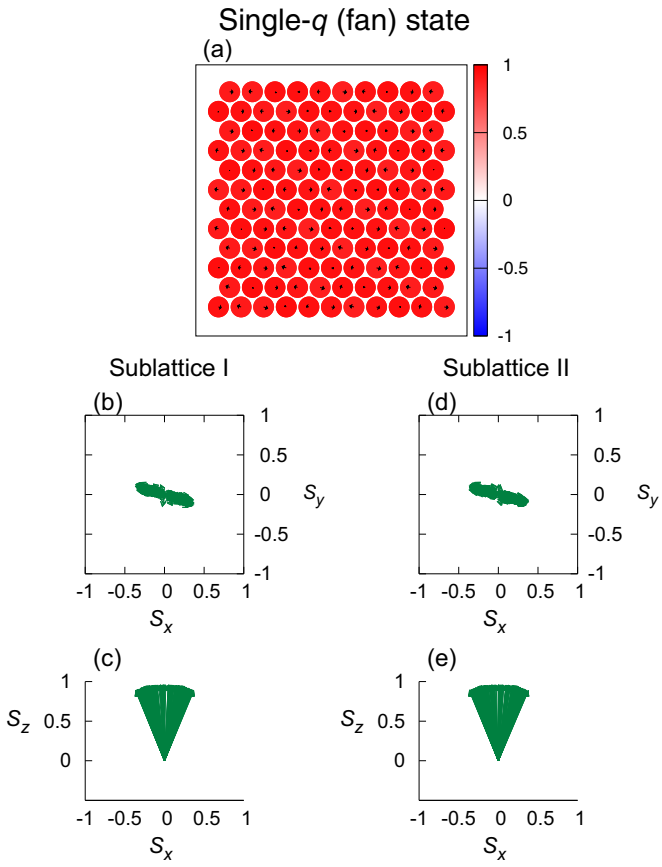

FIG. 10. Real-space sublattice spin configurations in the single-q (fan) state for $J_2/J_1 = 0.3$ obtained by the short-time average of 1000 MC steps: (a)–(c) for the sublattice I and (d) and (e) for the sublattice II. The parameters are $H/|J_1| = 6.0$, $T/|J_1| = 0.003862$, and $L = 150$. (a) The xy components of the spin are represented by the arrow, while the z component is represented by the blue-to-red color scale. In (b)–(e), spins at various sites on a given sublattice are reorganized with a common origin: [(b) and (d)] the top view in the (S_x, S_y) plane and [(c) and (e)] the side view in the (S_x, S_z) plane.

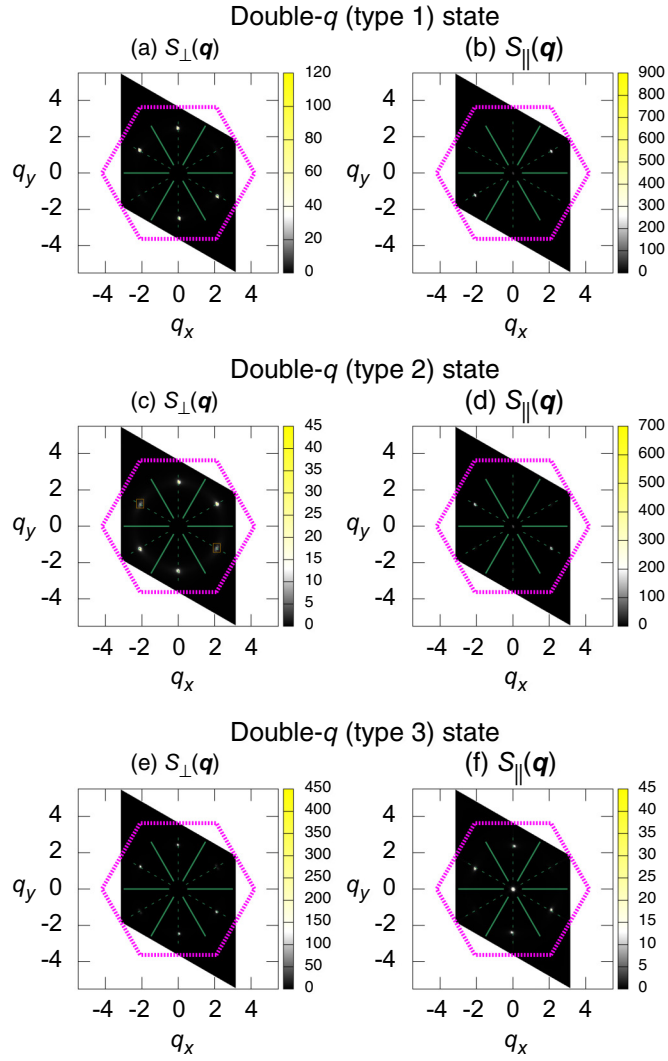

FIG. 11. The intensity plots of the sublattice spin structure factors in the wave-vector (q_x, q_y) plane in various type of double-q states at $J_2/J_1 = 0.3$: [(a), (c), and (e)] the transverse component $S_\perp(\mathbf{q})$ and [(b), (d), and (f)] the longitudinal component $S_\parallel(\mathbf{q})$. The parameters are $H/|J_1| = 1.5$, $T/|J_1| = 0.017$, and $L = 108$ for (a) and (b), $H/|J_1| = 1.5$, $T/|J_1| = 0.025$, and $L = 108$ for (c) and (d), and $H/|J_1| = 2.5$, $T/|J_1| = 0.027$, and $L = 150$ for (e) and (f).

In fact, this double-q (type 1) state is essentially the same state as the double-q state observed in the triangular-lattice Heisenberg model in Ref. [33]. The state can be regarded as the superposition of the two spirals in the xy component and the lineally polarized spin density wave in the z component. Its real-space sublattice spin configurations corresponding to the spin structure factor shown in Figs. 11(a) and 11(b) are given in Figs. 12(a) and 12(b) for the two sublattices.

D. The double-q (type 2) state

Next, we move to the second type of double-q states, the double-q (type 2) state. The corresponding intensity plots of the sublattice spin structure factors are given in Figs. 11(c) and 11(d). Note that six peaks appear in the xy component of the static spin structure factors shown in Figs. 11(c), while two of them indicated in Fig. 11(c) are just broad peaks with weaker intensity than the other four peaks, about 52% weaker in intensity, spontaneously breaking the sixfold rotational symmetry. As can be seen from Figs. 11(c) and 11(d), the associated wave vectors run along the NN directions. Hence, overall features of the static spin structure in this double-q (type 2) state are similar to those in the double-q (type 1) state. The real-space spin configuration, however, are very different. We show in Figs. 13(a) and 13(b) the real-space spin configurations in the double-q (type 2) state, (a) for the sublattices I, and (b) for the sublattice II. In Figs. 13(c)–13(f), spins at various sites on the sublattice I [(c) and (d)] and on the sublattice II [(e) and (f)] are reorganized with a common origin. As can be seen from the figures, the double-q (type 2) state has a coplanar structure in real space, spins lying on a plane containing the magnetic-field (z) axis, in contrast to the noncoplanar structure of the double-q (type 1) state.

E. The double-q (type 3) state

Still another type of double-q state, the double-q (type 3) state, is also possible, which actually occupies a rather

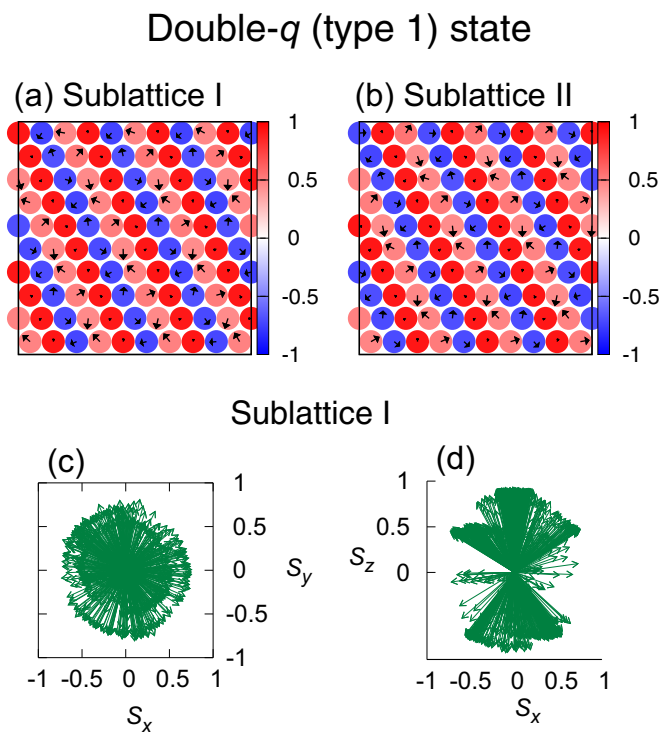

FIG. 12. Real-space sublattice spin configurations in the double-q (type 1) state obtained by short-time average of 400 MC steps: (a) for the sublattice I and (b) for the sublattice II. The parameters are $J_2/J_1 = 0.3$, $H/|J_1| = 1.5$, $T/|J_1| = 0.017$, and $L = 108$. [(a) and (b)] The xy components of the spin are represented by the arrow, while the z component is represented by the blue-to-red color scale. In (c) and (d), spins at various sites on the sublattice I are reorganized with a common origin: (c) the top view in the (S_x, S_y) plane and (d) the side view in the (S_x, S_z) plane.

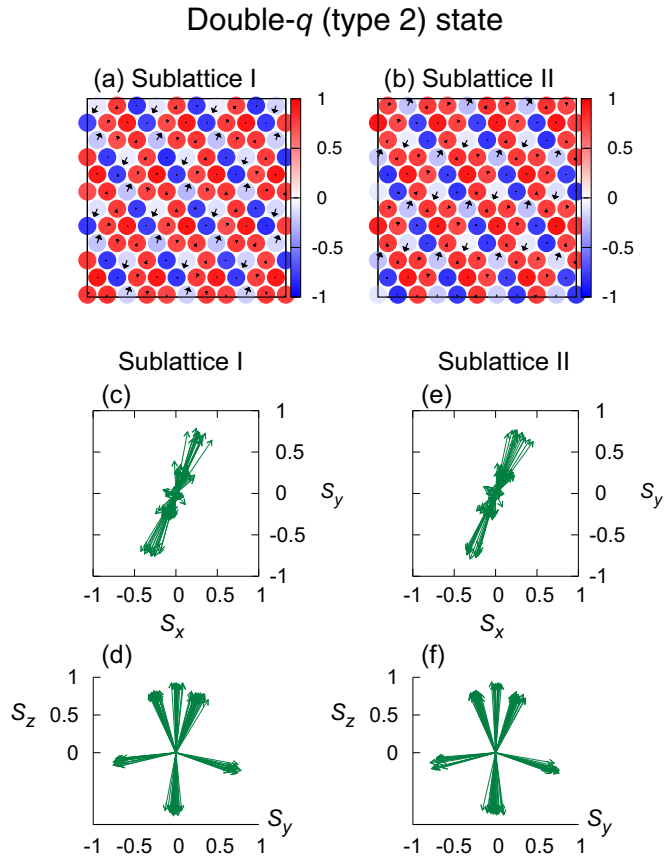

FIG. 13. Real-space sublattice spin configurations in the double-q (type 2) state obtained by the short-time average of 100 MC steps: (a) for the sublattice I and (b) for the sublattice II. The parameters are $J_2/J_1 = 0.3$, $H/|J_1| = 1.5$, $T/|J_1| = 0.025$, and $L = 200$. [(a) and (b)] The xy components of the spin are represented by the arrow, while the z component is represented by the blue-to-red color scale. In (c)–(f), spins at various sites on the sublattice I [(c) and (d)] and II [(e) and (f)] are reorganized with a common origin: [(c) and (e)] the top view in the (S_x, S_y) plane, and [(d) and (f)] the side view in the (S_y, S_z) plane.

wide region of the phase diagram of Fig. 3. The typical intensity plots of the double-q (type 3) state are shown in Figs. 11(e) and 11(f). Unlike the double-q states of type 1 or 2, the peaks of $S_\parallel(\mathbf{q})$ appear at the same two-pair positions as those of $S_\perp(\mathbf{q})$. Indeed, a closer inspection has revealed that the ordering wave vectors at the double-q (type 3) state have features different from those of the other double-q states (type 1 and type 2). In Figs. 14(a) and 14(b), we show the intensity plots of both (a) $S_\perp(\mathbf{q})$ and (b) $S_\parallel(\mathbf{q})$, focused around one given spot located near the q_y axis corresponding to the NN direction of the honeycomb lattice, together with the curve of the degenerate ring. As can be seen from the figures, the peak positions of $S_\perp(\mathbf{q})$ and of $S_\parallel(\mathbf{q})$ differ somewhat, both being off lines from the NN direction in mutually opposite directions. Hence, wave vectors in the double-q (type 3) state are actually composed of four individual wave vectors. Furthermore, both peak positions deviate even from the degenerate ring, the $|q^*|$ value being smaller than the degenerate-ring radius by about 2% in $S_\perp(\mathbf{q})$ and by about 4% in $S_\parallel(\mathbf{q})$. In fact, the deviation of the $|q^*|$ value from the degenerate ring is also seen for other states due to the effects of thermal fluctuations, though by the same amount between in $S_\perp(\mathbf{q})$ and in $S_\parallel(\mathbf{q})$.

To further examine the nature of the ordering, we show in Figs. 14(c) and 14(d) the size dependence of the $S_\perp(\mathbf{q})$ and $S_\parallel(\mathbf{q})$ peaks. As can be seen from the figure, the peak positions clearly differ in $|q|$ between in $S_\perp(\mathbf{q})$ and in $S_\parallel(\mathbf{q})$. On increasing the lattice size L, the peak of $S_\perp(\mathbf{q})$ tends to sharpen, which seems consistent with the expected quasi-LRO of the xy components: remember that the xy spin components possess the U(1) [or SO(2)] symmetry around the z axis under the magnetic field. A similar behavior is observed in the size dependence of the peak height of $S_\parallel(\mathbf{q})$ suggesting the existence of the quasi-LRO also in the longitudinal component.

The real-space spin configurations in the double-q (type 3) state are shown in Figs. 15(a) and 15(b) for the sublattice I and Figs. 15(c)–15(f) for the sublattice II. The spin configurations are shown in (a) and (c) and in (b) and (d), each set representing two different spatial regions in the same sample. As can be seen from the figures, the xy-spin components form interweaving vortex/antivortex lattice patterns. The state shown in Fig. 15(a) looks like a periodic array of vortices as highlighted by the circled regions in the figure, while antivortexlike spin configurations are formed in the regions between the vortices. Likewise, the state shown in Fig. 15(b)

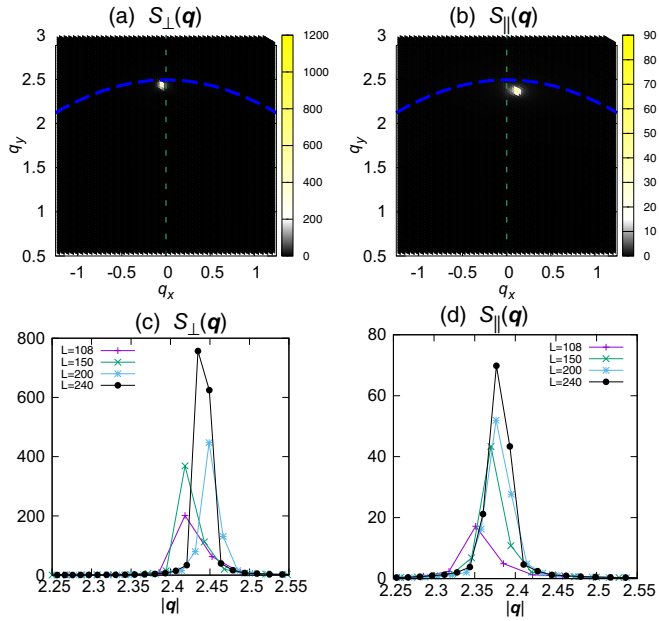

FIG. 14. The intensity plots of the sublattice spin structure factors in the double-q (type 3) state focused around one spot located close to the q_y axis: for (a) the transverse component $S_\perp(\mathbf{q})$ and (b) for the longitudinal component $S_\parallel(\mathbf{q})$. The parameters are $J_2/J_1 = 0.3$, $H/|J_1| = 2.5$, $T/|J_1| = 0.027$, and $L = 240$. The blue dotted curve represents the degenerate ring corresponding to $J_2/J_1 = 0.3$ as shown in Fig. 2. The wave-vector $|\mathbf{q}|$ dependence of the static spin structure factor peaks of (c) the transverse component $S_\perp(\mathbf{q})$, and (d) the longitudinal component $S_\parallel(\mathbf{q})$, measured along the line passing the peak position in the NN direction. The parameters are $J_2/J_1 = 0.3$, $H/|J_1| = 2.5$, and $T/|J_1| = 0.02708$ for the lattice sizes $L = 108,\ 150,\ 200$, and 240.

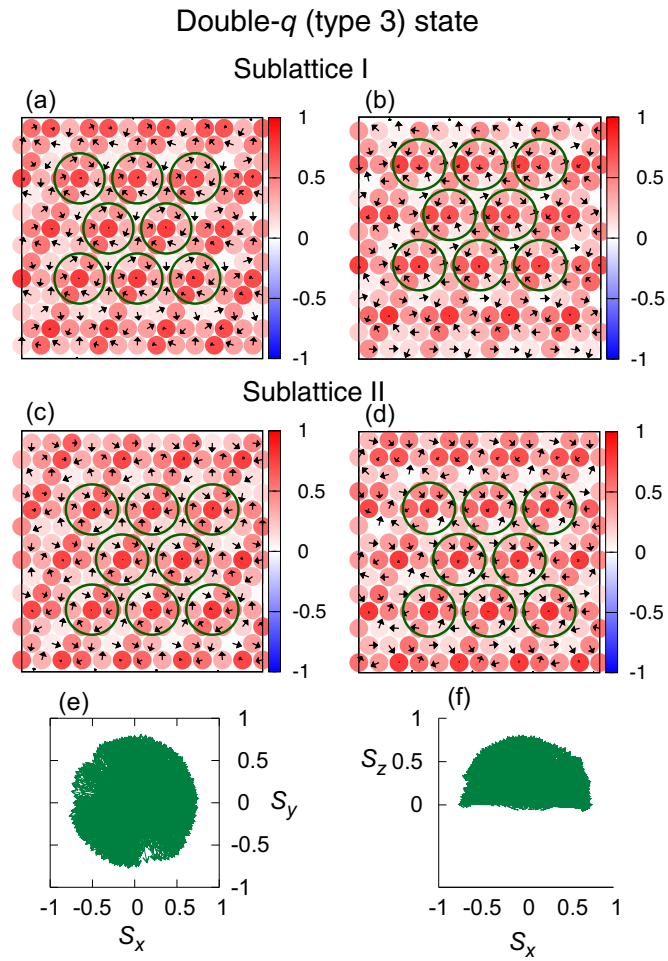

FIG. 15. [(a) and (b)] The real-space sublattice spin configurations of the double-q (type 3) state obtained by the short-time average of 1000 MC steps: [(a) and (b)] for the sublattice I and (c)–(f) for the sublattice II. The parameters are $J_2/J_1 = 0.3$, $H/|J_1| = 2.5$, $T/|J_1| = 0.027$, and $L = 240$. The spin configurations are shown in (a) and (c) and in (b) and (d), each set representing two different spatial regions in the same sample. The xy components of the spin are represented by the arrow, while the z component is represented by the blue-to-red color scale. In (e) and (f), spins at various sites on the sublattice II are reorganized with a common origin: (e) the top view in the (S_x, S_y) plane and (f) the side view in the (S_x, S_z) plane.

looks like a periodic array of antivortices, while vortexlike spin configurations are formed in the regions between the antivortices. The vortex-lattice-looking region on the sublattice I [Fig. 15(a)] looks like the vortex lattice also on the sublattice II with some phase shift [Fig. 15(c)], and the antivortex-lattice-looking region on the sublattice I [Fig. 15(b)] looks like the antivortex-lattice also on the sublattice II with some phase shift [Fig. 15(d)]. The reason why the vortex-lattice-looking region and the antivortex-lattice-looking region spatially alternates in the same sample is simply because the $\mathbf{q}$ value associated with the present vortex/antivortex lattice state is incommensurate with the underlying triangular sublattice, and the relative phase difference gradually modulates from lattice point to lattice point. Indeed, the $|\mathbf{q}|$ value associated with the present vortex/antivortex order is $|\mathbf{q}| \simeq 2.43$ as can be seen from Fig. 14(c), slightly off the threefold commensurate value of $|\mathbf{q}| = 4\pi/3\sqrt{3} \simeq 2.418$.

In Figs. 15(e) and 15(f), spins on one sublattice at various sites are reorganized in the spin space with a common origin: a top view in the (S_x, S_y) plane in (e) and a side view in the (S_x, S_z) plane in (f). One can see from Fig. 15(f) that the spin texture does not cover a whole sphere, only a half sphere being mapped like a half-skyrmion or "meron" [48–50]. The meronlike structure arises from the modulation of the spin z component characterized by $\mathbf{q}^*$ observed in $S_\parallel(\mathbf{q})$. Hence, the sublattice spin structure in the double-q (type 3) state is a meron/antimeronlike lattice rather than the vortex/antivortex lattice.

F. The triple-q (collinear) state

We now move to the triple-q state. We find only one type of triple-q state in our model with J_2/J_1=0.3, the triple-q (collinear) state. The corresponding sublattice spin structure factors are shown in Fig. 16. $S_\parallel(\mathbf{q})$ exhibits sharp peaks of equal intensities at all $\mathbf{q}^*$ wave vectors in the NN directions, keeping the C_3 lattice symmetry. The observation is consistent with the behavior of the m_3 order parameter shown in Fig. 4(b). $S_\perp(\mathbf{q})$ also exhibits peaks at the same positions as the ones of $S_\parallel(\mathbf{q})$, while they remain very broad, suggesting only a weak SRO developed in the xy-spin component. The

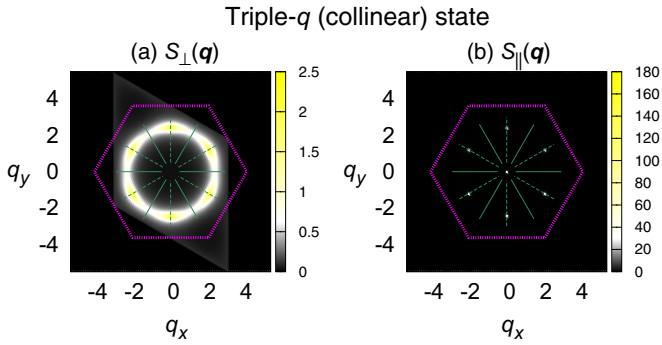

FIG. 16. The intensity plots of the sublattice spin structure factors in the wave-vector (q_x, q_y) plane in the triple-q (collinear) state: (a) the transverse component $S_\perp(\mathbf{q})$ and (b) the longitudinal component $S_\parallel(\mathbf{q})$. The parameters are $J_2/J_1 = 0.3$, $H/|J_1| = 1.10$, $T/|J_1| = 0.03617$, and $L = 108$.

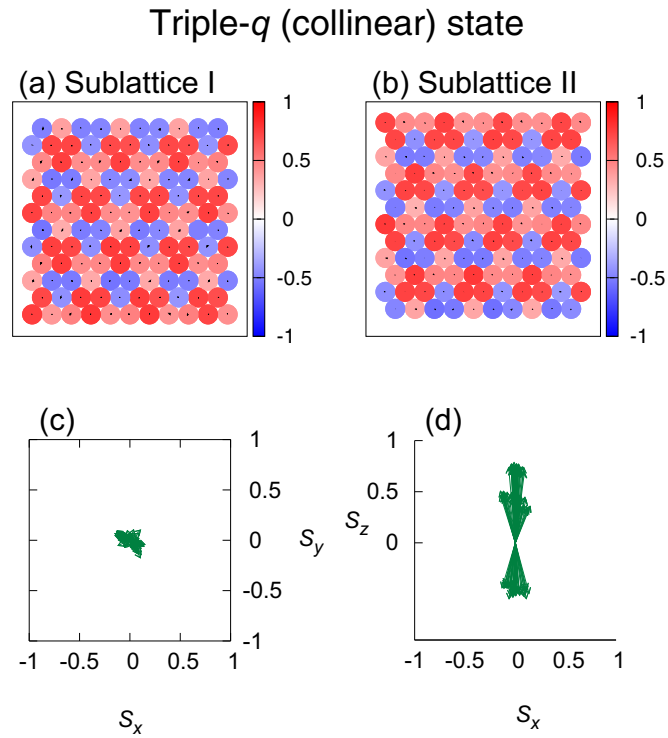

FIG. 17. Real-space sublattice spin configurations in the triple-q (collinear) state obtained by the short-time average of 1000 MC steps: (a) for the sublattice I and (b) for the sublattice II. The parameters are $J_2/J_1 = 0.3$, $H/|J_1| = 1.5$, $T/|J_1| = 0.03778$, and $L = 200$. The xy components of the spin are represented by the arrow, while the z component is represented by the blue-to-red color scale. In (c) and (d), spins at various sites on the sublattice I are reorganized with a common origin: (c) the top view in the (S_x, S_y) plane and (d) the side view in the (S_x, S_y) plane. Essentially the same figure is obtained also for the sublattice II.

degenerate ringlike structure characteristic of the ring-liquid paramagnetic state is still clearly visible in $S_\perp(\mathbf{q})$, suggesting the remanence of enhanced fluctuations similar to those of the ring-liquid state. As already mentioned, from the symmetry viewpoint, this collinear state is adiabatically identical with the Z state observed in the triangular model [33].

A typical real-space spin configurations in the triple-q (collinear) state are shown in Fig. 17: (a) for the sublattice I and (b) for the sublattice II. As can be seen from the figures, the spin z component on each sublattice forms a super-triangular-lattice pattern, while the spin xy components remain disordered, leading to the collinear spin ordering. The spin z-component configurations on the two sublattices turn out to be essentially similar, their apparent difference borne by appropriate phase factors between the sublattices I and II. Namely, each of the triple-q wave vectors, q_1^*, q_2^* and q_3^*, possesses associated phase factors, $\alpha_{q_1^*}$, $\alpha_{q_2^*}$ and $\alpha_{q_3^*}$, which are not necessarily equal with each other, reflecting our choice of the unit cell indicated in Fig. 1, which apparently breaks the lattice C_3 symmetry. Some more information of the MF level is given in Ref. [42].

The triple-q (collinear) state is realized in the phase diagram only at relative high temperatures and at the intermediate field, say, around $H/J_1 \simeq 1.5$. In fact, the ordering behaviors at this intermediate field turns out to be quite rich, as can be seen from the H-T phase diagram of Fig. 3. Namely, on decreasing the temperature from the ring-liquid paramagnetic state, the system first enters into the collinear triple-q state, then into the noncollinear but coplanar double-q state [double-q (type 2) state], then into the noncoplanar double-q state [double-q (type 1) state], and eventually into the noncoplanar single-q (NN) state at low enough temperatures.

In concluding this section, we comment on our MF analysis very briefly. In order to clarify the origin of the various multiple-q states observed in this section, we also perform a MF analysis following the methods of Reimers *et al.* [46] and of Okubo *et al.* [32,33]. The details are given in Ref. [42]. Note that our MF analysis have some limitations in accuracy since it completely neglects fluctuations. Furthermore, as we have used the knowledge of the static spin structure factors obtained from our MC simulations in finding the possible solutions of the MF equation, we cannot rule out any state other than the ones reported here as saddle-point MF solutions. As a stable state, our MF analysis always yields only the umbrella-type single-q state in contrast to the richness of the phase diagram of Fig. 3. This inadequacy is due to the neglected fluctuations. The energy scale associated with the ordering at the MF level is an order of magnitude greater than the true transition temperature T_c determined by MC. Though T_c generally tends to be over-estimated in any MF analysis due to its negligence of fluctuations, the extent of the over-estimation is quite remarkable in the present case. This is probably due to the ringlike degeneracy where many possible wave vectors compete, which is again neglected in the present MF analysis. However, we succeed in obtaining all ordered state observed in our MC simulation, at least as the saddle-point solutions of the MF equations. It then turns out that the umbrella-type single-q is the only stable solution and the all other states are just the saddle-point solutions, indicating that the umbrella-type single-q state is always stabilized at the MF level. This observation highlights the crucial importance of fluctuations in stabilizing the various multiple-q states in the present honeycomb-lattice system. The MF analysis also provides us some useful information about, e.g., the running direction of the wave vector chosen from the degenerate ring, the relative relationship between

the phase factors in each multiple-q state, as well as the convenient compact expressions of the spin configurations describing the spin configurations in each multiple-q state, etc., even when the multiple-q states are not true stable states at the MF level.

IV. OTHER VALUES OF J_2/J_1

In the previous section, we have focused on the case of $J_2/J_1 = 0.3$. There, the ordering behavior has turned out to be quite rich, including a variety of multiple-q states. In this section, we touch upon the ordering behavior of the model for other J_2/J_1-values in the range $1/6 < J_2/J_1 < 0.5$, i.e., $J_2/J_1 = 0.20$, 0.25, 0.35, and 0.45. We find that, unlike the case of $J_2/J_1 = 0.30$, most of the H-T phase diagrams consists of umbrella-type single-q states, as shown in Fig. 18, being qualitatively similar to the MF phase diagram (see Ref. [42]). Exceptions might be that, for $J_2/J_1 = 0.25$, the triple-q (collinear) state appears in a narrow part of the phase diagram, and that, for $J_2/J_1 = 0.45$, two kinds of triple-q states possessing different spin configurations from that in the triple-q (collinear) state, are stabilized. In fact, $J_2/J_1 = 0.45$ is close to the border line value $J_2/J_1 = 0.50$ at which the degenerate ring coincides with the first Brillouin zone (BZ) boundary, where underlying physics might be related to the BZ boundary. The two triple-q states observed at $J_2/J_1 = 0.45$ are the "3-1 triple-q state" and "collinear 3-1 triple-q state" already reported in Ref. [19] for $J_2/J_1 = 0.5$. The 3-1 triple-q state is not a collinear state different in nature from the triple-q (collinear) state realized at $J_2/J_1 = 0.3$ and 0.25. On the other hand, we find that the spin configuration in the collinear 3-1 triple-q state, shown in Appendix B, can be described by the same equation as in the triple-q (collinear) state (see Eq. (33) in Ref. [42]). The apparent difference in their spin configurations comes only from the length of the ordering wave vectors on the associated degenerate ring.

We also comment that the emergence of an infinituple-q ordered state called a "ripple state" was recently reported in Ref. [51] for the system of $J_2/J_1 = 0.18$ lying close to the AF phase boundary.

V. SUMMARY AND DISCUSSION

In summary, we have investigated the ordering behaviors of the frustrated J_1-J_2 classical honeycomb-lattice Heisenberg AF under a magnetic field. Special attention has been paid to the case of $J_2/J_1 = 0.3$, which is located in the middle of the paramagnetic (ring-liquid)-helical phase boundary. The ringlike continuous degeneracy, and the resulting paramagnetic ring-liquid state provides a matrix of a rich variety of multiple-q ordered states stabilized under the field.

Via extensive MC simulations on the model, we have found a variety of multiple-q states including the single-q, the double-q, and the triple-q states, also including the noncoplanar, coplanar and collinear states. In contrast to the triangular-lattice case, the triple-q skyrmion-lattice state is not stabilized. In fact, the obtained H-T phase diagram turns out to differ considerably from that of the corresponding triangular-lattice model.

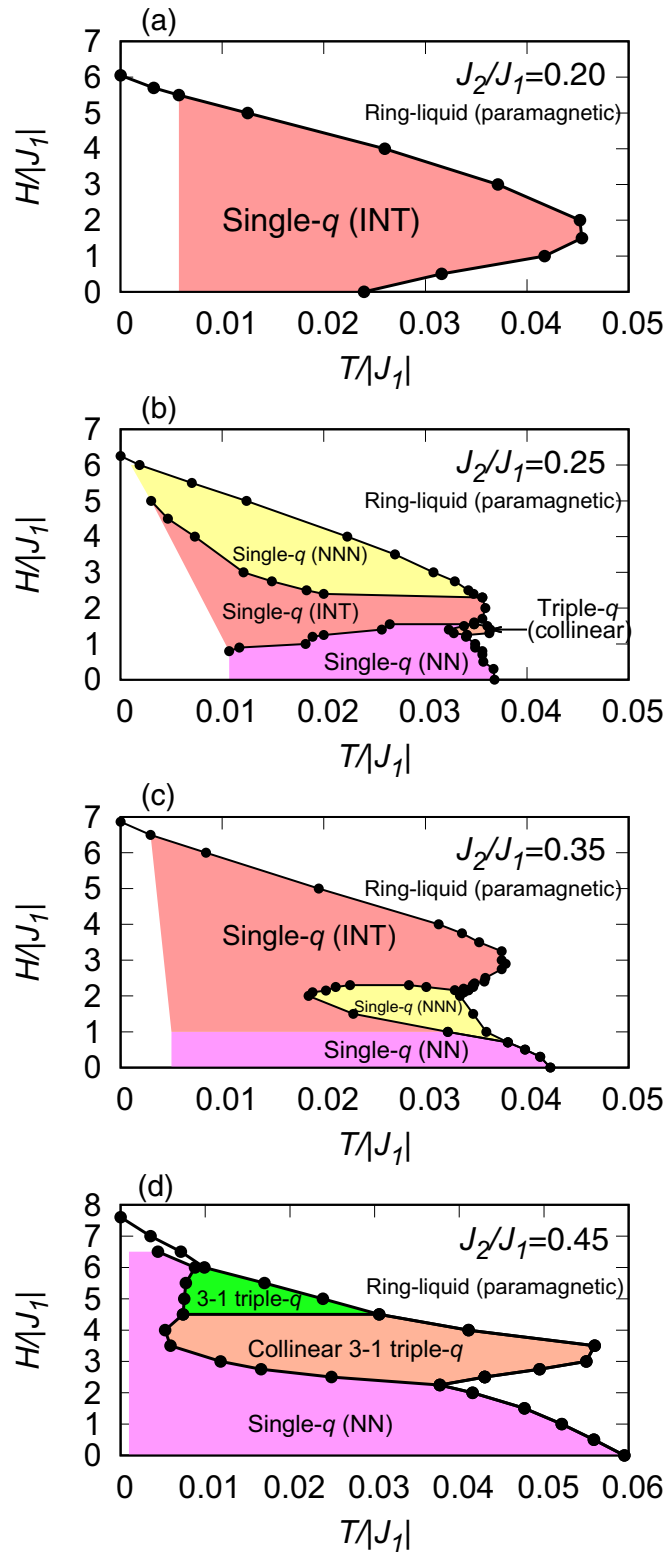

FIG. 18. The H-T phase diagrams for $J_2/J_1 = 0.20$, 0.25, 0.35, and 0.45 obtained by MC simulations. Transition points denoted by black dots are determined from the specific-heat peak.

For single-q states, the umbrella-type and the fan-type single-q states are found, the latter being stabilized only in high field. The umbrella-type single-q state occupies a wide region in the H-T phase diagram, which might be further

divided into several types of phases depending on the running direction of the associated q vector. In the low-temperature limit, the q vector running along the NN direction is preferred irrespective of the filed intensity for $J_2/J_1 = 0.3$ as is indicated by the low-temperature expansion calculation, whereas at higher temperatures the q vector sometimes runs along the NNN direction or along the intermediate direction between NN and NNN.

In addition to these single-q states, three distinct types of double-q states, i.e., the type 1, 2, and 3 double-q states, are identified. The double-q (type 1) state is similar to the double-q state of the triangular-lattice model. It is a noncoplanar state with the double-q structure in the xy plane, forming the linearly polarized spin-density wave along the z direction. The double-q (type 2) state is a coplanar state where spins lie on a plane containing the z axis. Particularly intriguing might be the double-q (type 3) state, which corresponds to an interweaving meron/antimeronlike lattice state.

The triple-q state realized in the present honeycomb model at $J_2/J_1 = 0.3$ is the collinear triple-q state in which the spin z component forms a superlattice structure incommensurate with the underlying honeycomb lattice and the translational symmetry is spontaneously broken. This collinear state is adiabatically identical with the "Z" state identified in the triangular-lattice model. In the latter state, the transverse spin correlation length turns out to be moderately long, which corresponds to the average domain size of the skyrmion (antiskyrmion) lattice domains. The triple-q skyrmion-lattice state, which was observed to be stabilized in the triangular model in the vicinity of its Z phase, turns out not to be stabilized in the present honeycomb model.

We also have investigated other J_2/J_1 values than $J_2/J_1 = 0.3$, to find that the dominant ordered state is an umbrella-type single-q state except for the case near $J_2/J_1 = 0.5$. The richness of the $J_2/J_1 = 0.3$ phase diagram might be related to the fact that the $J_2/J_1 = 0.3$ point is located in the midst of the ring-liquid state in the J_2/J_1-T phase diagram, as shown by Okumura *et al.* in Ref. [6] (see its Fig. 9). In a wider parameter region of $0.2 \leqslant J_2/J_1 \leqslant 0.45$, we have observed switching behaviors of the running directions of the critical wave vector in single-q states as a function of the magnetic field and the temperature, which is likely to be a universal character of the honeycomb-lattice system.

Finally, we wish to discuss possible implications of our present results to real magnets. One candidate material might be the $S = 3/2$ honeycomb-lattice Heisenberg antiferromagnet $Bi_3Mn_4O_{12}(NO_3)$ [26–31]. Spin-liquidlike behavior was reported for this material in zero field, together with the field-induced antiferromagnetism. Further comprehensive experimental study of its in-field properties and the magnetic phase diagram might be interesting. This material actually consists of stacked honeycomb bilayers, with the AF coupling between the two honeycomb layers. In comparing the present results with experiments especially under the field, care needs to be taken.

The other candidate material might be a quantum bilayer kagome material $Ca_{10}Cr_7O_{28}$, which was revealed to exhibit a spin-liquidlike behavior [52,53]. It was suggested that $Ca_{10}Cr_7O_{28}$ might be modeled as a semiclassical honeycomb-lattice Heisenberg model with the ferromagnetic NN and the antiferromagnetic NNN interactions [54,55]. This material exhibits a ring-liquidlike behavior with a characteristic ringlike pattern in the associated neutron scattering signal [54,55]. Although J_1 is ferromagnetic in this material distinct from the one studied here, some of the ordering features may be common. Further study is desirable to clarify the situation.

Finally, we wish to emphasize that the ringlike degeneracy and the resulting ring-liquid state could be a source of various exotic multiple-q states. This is true not only in the present honeycomb-lattice system, but also in other systems with different lattice geometries, e.g., a square-lattice system having a ringlike degeneracy in its ground state was reported to exhibit a vortex crystal state in Ref. [38]. Another example might be a three-dimensional diamond-lattice system having a surfacelike degeneracy [4], which was reported to give rise to different types of multiple-q states [56].

We hope that our present theoretical studies on a simple honeycomb model could provide a step toward the fuller understanding of rich ordering behaviors exhibited frustrated honeycomb magnets, or more generally, frustrated magnets possessing a massive ground-state degeneracy.

ACKNOWLEDGMENTS

The authors are pleased to acknowledge helpful conversation with S. Okumura in early stages of this study. The authors, are thankful to R. Pole, H. Yan and N. Shannon for fruitful discussions including the one about the recent new material $Ca_{10}Cr_7O_{28}$. The authors are thankful to ISSP, the University of Tokyo and OIST for providing us with CPU time. This study is supported by Grant-in-Aid for Scientific Researchs No. 19K14665, No. 19K03740, No. 25247064, No. 17H06137, and No. 15K17701.

APPENDIX A: LOW-TEMPERATURE EXPANSION

In this Appendix, we explain some of the details of the low-temperature expansion. Our low-temperature expansion is performed following the method described in Refs. [4,6]. The partition function Z of the model with the Hamiltonian H

$$Z = \int D\mathbf{S} e^{-\beta\mathcal{H}} \prod_{j=1}^{N} \delta\left[\mathbf{S}_j^2 - 1\right], \tag{A1}$$

is evaluated by the low-temperature expansion from an arbitrary state on the degenerate ring as an unperturbed state. The fixed spin-length condition of the classical system requires that the ground state of the model is a single-q state, and we assume as a ground state under the magnetic field an umbrellalike state given by

$$\overline{\mathbf{S}}_n^a = \left(\sqrt{1 - m_z'^2}\cos\theta_n^a, \sqrt{1 - m_z'^2}\sin\theta_n^a, m_z'\right) \tag{A2}$$

$$\theta_n^a = \mathbf{q}^* \cdot \mathbf{r}_n + \alpha_{\mathbf{q}^*}\delta_{a\mathrm{II}}, \tag{A3}$$

where $\mathbf{r}_n$ is the position vector of the unit cell n, a is the label for the two sublattices ($a = \mathrm{I}$ or II), $\mathbf{q}^*$ denotes the incommensurate spiral wave vector in the xy plane, and $\alpha_{\mathbf{q}}$ denotes the sublattice phase difference as defined by Eq. (6) of Ref. [42]. The spin longitudinal component m' is

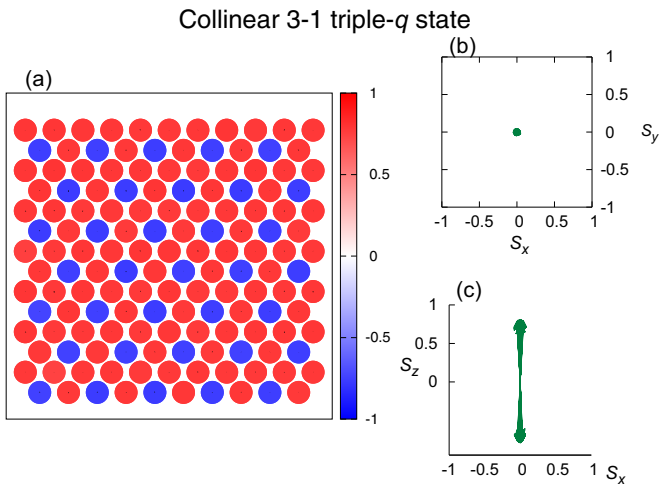

FIG. 19. Real-space sublattice spin configuration in the collinear 3-1 triple-q state obtained by the short-time average of 1000 MC steps. The parameters are $J_2/J_1 = 0.45$, $H/|J_1| = 3.0$, $T/|J_1| = 0.04006$, and $L = 120$ under periodic boundary conditions. (a) The xy components of the spin are represented by the arrow, while the z component is represented by the blue-to-red color scale. In (b) and (c), spins at various sites on a given sublattice are reorganized with a common origin: (b) the top view in the (S_x, S_y) plane and (c) the side view in the (S_x, S_z) plane.

obtained as

$$m_z' = \frac{H}{\lambda_{\mathbf{q}^*}^+ - \lambda_{\mathbf{0}}^-}, \tag{A4}$$

where the $\lambda_{\mathbf{q}}^{\pm}$ are the eigenvalues of the Hamiltonian given in Eq. (10) of Ref. [42].

Let us introduce the deviation vector $\boldsymbol{\pi}_n^a$, which satisfies $\boldsymbol{\pi}_n^a \perp \overline{\mathbf{S}}_n^a$. Then, we have

$$\mathbf{S}_n^a = \boldsymbol{\pi}_n^a + \overline{\mathbf{S}}_n^a \sqrt{1 - \pi_j^2}. \tag{A5}$$

The plane perpendicular to $\overline{\mathbf{S}}_n^a$ can be spanned by the two orthogonal unit vectors $\mathbf{e}_\perp$ and $\mathbf{e}_\perp \times \overline{\mathbf{S}}_n^a$, where

$$\mathbf{e}_\perp = \left(-m_z' \cos\theta_n^a, -m_z' \sin\theta_n^a, \sqrt{1 - m_z'^2}\right). \tag{A6}$$

We decompose the vector $\boldsymbol{\pi}_n^a$ as

$$\boldsymbol{\pi}_n^a = \phi_n^a \mathbf{e}_\perp + \chi_n^a \left[\mathbf{e}_\perp \times \overline{\mathbf{S}}_n^a\right] \tag{A7}$$

and expand the Hamiltonian up to the quadratic order both in χ and ϕ. The partition function Z can be written as

$$Z = \int \prod_{n,a} d\phi_n^a d\chi_n^a e^{-\beta \mathcal{H}}. \tag{A8}$$

which can be evaluated by the Gaussian integrals. Neglecting the terms independent of the critical wave vector $\mathbf{q}^*$, we finally get the following expression of the $\mathbf{q}^*$-dependent part of the free energy density,

$$F(\mathbf{q}^*)/T \sim \int d\mathbf{q} \{\ln[-(W_{\mathrm{I,I}} + |W_{\mathrm{I,II}}|)] + \ln[-(W_{\mathrm{I,I}} - |W_{\mathrm{I,II}}|)]\}, \tag{A9}$$

where

$$\begin{aligned} W_{\mathrm{I,I}}(\mathbf{q}^*, \mathbf{q}) &= 2J_2 \Big\{ \left[\left(1 - m_z'^2\right)\cos(\mathbf{q}^* \cdot \mathbf{a}_x) + m_z'^2\right]\cos(\mathbf{q} \cdot \mathbf{a}_x) \\ &+ \left[\left(1 - m_z'^2\right)\cos(\mathbf{q}^* \cdot \mathbf{a}_y) + m_z'^2\right]\cos(\mathbf{q} \cdot \mathbf{a}_y) \\ &+ \left[\left(1 - m_z'^2\right)\cos(\mathbf{q}^* \cdot (\mathbf{a}_x - \mathbf{a}_y)) + m_z'^2\right] \\ &\times \cos(\mathbf{q} \cdot (\mathbf{a}_x - \mathbf{a}_y))\Big\} - \lambda_+(\mathbf{q}^*), \end{aligned} \tag{A10}$$

$$\begin{aligned} W_{\mathrm{I,II}}(\mathbf{q}^*, \mathbf{q}) = J_1 \Big\{ &\left[\left(1 - m_z'^2\right)\cos\alpha_{\mathbf{q}^*} + m_z'^2\right] \\ &+ \left[\left(1 - m_z'^2\right)\cos(\mathbf{q}^* \cdot \mathbf{a}_x - \alpha_{\mathbf{q}^*}) + m_z'^2\right] e^{i\mathbf{q}\cdot\mathbf{a}_x} \\ &+ \left[\left(1 - m_z'^2\right)\cos(\mathbf{q}^* \cdot \mathbf{a}_y - \alpha_{\mathbf{q}^*}) + m_z'^2\right] e^{i\mathbf{q}\cdot\mathbf{a}_y}\Big\}. \end{aligned} \tag{A11}$$

When m_z'=0, these equations reduce to the ones given in Appendix of Ref. [6].

APPENDIX B: THE COLLINEAR 3-1 TRIPLE-q STATE

We present the real-space sublattice spin configuration for the collinear 3-1 triple-q state observed for $J_2/J_1 = 0.45$, as given in Fig. 19. We find that this spin configuration can be reproduced by Eq. (35) of Ref. [42], that means, the same equation of the triple-q (collinear) state observed for the $J_2/J_1 = 0.3$, with the ordering wave vectors on the degenerate ring corresponding to $J_2/J_1 = 0.45$.

[1] J. Villain, R. Bidaux, J. P. Carton, and R. Conte, J. Phys. (Paris) **41**, 1263 (1980).
[2] H. Kawamura, J. Phys. Soc. Jpn. **53**, 2452 (1984).
[3] C. L. Henley, Phys. Rev. Lett. **62**, 2056 (1989).
[4] D. Bergman, J. Alicea, E. Gull, S. Trebst, and L. Balents, Nat. Phys. **3**, 487 (2007).
[5] S. Katsura, T. Ide, and T. Morita, J. Stat. Phys. **42**, 381 (1986).
[6] S. Okumura, H. Kawamura, T. Okubo, and Y. Motome, J. Phys. Soc. Jpn. **79**, 114705 (2010).
[7] A. Mulder, R. Ganesh, L. Capriotti, and A. Paramekanti, Phys. Rev. B **81**, 214419 (2010).
[8] B. K. Clark, D. A. Abanin, and S. L. Sondhi, Phys. Rev. Lett. **107**, 087204 (2011).
[9] H. Mosadeq, F. Shahbazi, and S. Jafari, J. Phys.: Condens. Matter **23**, 226006 (2011).
[10] D. C. Cabra, C. A. Lamas, and H. D. Rosales, Phys. Rev. B **83**, 094506 (2011).
[11] R. Ganesh, D. N. Sheng, Y.-J. Kim, and A. Paramekanti, Phys. Rev. B **83**, 144414 (2011).
[12] J. Reuther, D. A. Abanin, and R. Thomale, Phys. Rev. B **84**, 014417 (2011).
[13] A. F. Albuquerque, D. Schwandt, B. Hetényi, S. Capponi,

M. Mambrini, and A. M. Läuchli, Phys. Rev. B **84**, 024406 (2011).
[14] R. F. Bishop, P. H. Y. Li, D. J. J. Farnell, and C. E. Campbell, J. Phys.: Condens. Matter **24**, 236002 (2012).
[15] F. Mezzacapo and M. Boninsegni, Phys. Rev. B **85**, 060402(R) (2012).
[16] P. H. Y. Li and R. F. Bishop, D. J. J. Farnell, and C. E. Campbell, Phys. Rev. B **86**, 144404 (2012).
[17] H. Zhang and C. A. Lamas, Phys. Rev. B **87**, 024415 (2013).
[18] R. F. Bishop, P. H. Y. Li, and C. E. Campbell, J. Phys.: Condens. Matter **25**, 306002 (2013).
[19] H. D. Rosales, D. C. Cabra, C. A. Lamas, P. Pujol, and M. E. Zhitomirsky, Phys. Rev. B **87**, 104402 (2013).
[20] S.-S. Gong, D. N. Sheng, O. I. Motrunich, and M. P. A. Fisher, Phys. Rev. B **88**, 165138 (2013).
[21] R. Ganesh, J. van den Brink, and S. Nishimoto, Phys. Rev. Lett. **110**, 127203 (2013).
[22] Z. Zhu, D. A. Huse, and S. R. White, Phys. Rev. Lett. **110**, 127205 (2013).
[23] S.-S. Gong, W. Zhu, D. N. Sheng, O. I. Motrunich, and M. P. A. Fisher, Phys. Rev. Lett. **113**, 027201 (2014).
[24] H. Zhang, M. Arlego, and C. A. Lamas, Phys. Rev. B **89**, 024403 (2014).
[25] S.-S. Gong, W. Zhu, and D. N. Sheng, Phys. Rev. B **92**, 195110 (2015).
[26] O. Smirnova M. Azuma, N. Kumada, Y. Kusano, M. Matsuda, Y. Shimakawa, T. Takei, Y. Yonesaki, and N. Kinomura, J. Am. Chem. Soc. **131**, 8313 (2009).
[27] M. Matsuda, M. Azuma, M. Tokunaga, Y. Shimakawa, and N. Kumada, Phys. Rev. Lett. **105**, 187201 (2010).
[28] S. Okubo, F. Elmasry, W. Zhang, M. Fujisawa, T. Sakurai, H. Ohta, M. Azuma, O. A. Sumirnova, and N. Kumada, J. Phys.: Conf. Ser. **200**, 022042 (2010).
[29] M. Azuma, M. Matsuda, N. Onishi, S. Olga, Y. Kusano, M. Tokunaga, Y. Shimakawa, and N. Kumada, J. Phys.: Conf. Ser. **320**, 012005 (2011).
[30] S. Okubo, T. Ueda, H. Ohta, W. Zhang, T. Sakurai, N. Onishi, M. Azuma, Y. Shimakawa, H. Nakano, and T. Sakai, Phys. Rev. B **86**, 140401(R) (2012).
[31] N. Onishi, K. Oka, M. Azuma, Y. Shimakawa, Y. Motome, T. Taniguchi, M. Hiraishi, M. Miyazaki, T. Masuda, A. Koda, K. M. Kojima, and R. Kadono, Phys. Rev. B **85**, 184412 (2012).
[32] T. Okubo, T. H. Nguyen, and H. Kawamura, Phys. Rev. B **84**, 144432 (2011).
[33] T. Okubo, S. Chung, and H. Kawamura, Phys. Rev. Lett. **108**, 017206 (2012).
[34] Y. Kamiya and C. D. Batista, Phys. Rev. X **4**, 011023 (2014).
[35] G. Marmorini and T. Momoi, Phys. Rev. B **89**, 134425 (2014).
[36] A. O. Leonov and M. Mostovoy, Nat. Commun. **6**, 8275 (2015).
[37] S.-Z. Lin and S. Hayami, Phys. Rev. B **93**, 064430 (2016).
[38] L. Seabra, P. Sindzingre, T. Momoi, and N. Shannon, Phys. Rev. B **93**, 085132 (2016).
[39] I. Rousochatzakis, U. K. Rössler, J. van den Brink, and M. Daghofer, Phys. Rev. B **93**, 104417 (2016).
[40] S. Hayami, S.-Z. Lin, and C. D. Batista, Phys. Rev. B **93**, 184413 (2016).
[41] L. Janssen, E. C. Andrade, and M. Vojta, Phys. Rev. Lett. **117**, 277202 (2016).
[42] See Supplemental Material at http://link.aps.org/supplemental/10.1103/PhysRevB.100.224404 for the details about the mean-field analysis.
[43] M. Creutz, Phys. Rev. D **36**, 515 (1987).
[44] K. Kanki, D. Loison, and K. D. Schotte, Eur. Phys. J. B **44**, 309 (2005).
[45] K. Hukushima and K. Nemoto, J. Phys. Soc. Jpn. **65**, 1604 (1996).
[46] J. N. Reimers, A. J. Berlinsky, and A.-C. Shi, Phys. Rev. B **43**, 865 (1991).
[47] M. E. Zhitomirsky, Phys. Rev. B **78**, 094423 (2008).
[48] D. J. Gross, Nucl. Phys. B **132**, 439 (1978).
[49] I. Affleck, Phys. Rev. Lett. **56**, 408 (1986).
[50] K. Moon, H. Mori, K. Yang, S. M. Girvin, A. H. MacDonald, L. Zheng, D. Yoshioka, and S.-C. Zhang, Phys. Rev. B **51**, 5138 (1995).
[51] T. Shimokawa and H. Kawamura, Phys. Rev. Lett. **123**, 057202 (2019).
[52] C. Balz, B. Lake, J. Reuther, H. Luetkens, R. Schonemann, T. Herrmannsdorfer, Y. Singh, A. T. M. N. Islam, E. M. Wheeler, J. A. Rodriguez-Rivera, T. Guidi, G. G. Simeoni, C. Baines, and H. Ryll, Nat. Phys. **12**, 942 (2016).
[53] C. Balz, B. Lake, A. T. M. Nazmul Islam, Y. Singh, J. A. Rodriguez-Rivera, T. Guidi, E. M. Wheeler, G. G. Simeoni, and H. Ryll, Phys. Rev. B **95**, 174414 (2017).
[54] S. Biswas and K. Damle, Phys. Rev. B **97**, 115102 (2018).
[55] R. Pohle, H. Yan, and N. Shannon, arXiv:1711.03778v1.
[56] S. Gao, O. Zaharko, V. Tsurkan, Y. Su, J. S. White, G. S. Tucker, B. Roessli, F. Bourdarot, R. Sibille, D. Chernyshov, T. Fennell, A. Loidl, and C. Rüegg, Nat. Phys. **13**, 157 (2017).